

A potential energy surface and a trajectory study of photodynamics and strong-field alignment of ClF molecule in rare gas (Ar,Kr) solids

Toni Kiljunen, Matias Bargheer,[†] Markus Gühr and Nikolaus Schwentner*

*Institut für Experimentalphysik, FU-Berlin, Arnimallee 14, D-14195 Berlin, Germany.
E-mail: nikolaus.schwentner@physik.fu-berlin.de*

*Received 24th November 2003, Accepted 24th February 2004
First published as an Advance Article on the web 31st March 2004*

Molecular alignment by a strong nonresonant laser pulse and a subsequent ultrafast pump–probe experiment are investigated by classical molecular dynamics simulations. A tendency to molecular alignment in the solid host in the presence of an intense ultrashort laser field is examined by simulating the external force due to the polarizability – field interaction. The ground state rotational potential of the ClF molecule is evaluated as the key determining factor along with the dynamics. The pump–probe scheme consists of time-delayed excitations $X\ ^1\Sigma_0^+ \rightarrow (B\ ^3\Pi_0 \text{ or } ^1\Pi_1) \rightarrow$ ionic states of ClF molecule in Ar or Kr crystals. We show the yields of dissociating ClF trajectories and discuss the fate of cage-exiting F atoms as a competing event to geminate recombination. Emphasis is put on the recombining trajectories. We extract the round-trip times and reorientations for the excited state “wave-packet” motion as important parameters for the analysis of the experimental photodynamics, and show the surrounding lattice response to the collisions.

I. Introduction

The active research field of ultrafast photoinduced processes is the general framework for our study.^{1–3} Steering a system from one state to another has a variety of applications, *e.g.*, from quantum computing, communications, and nuclear magnetic resonance to the case of the present study: molecular dynamics. For molecules, one tries to affect their photochemistry with high precision. Provided that chemical reaction mechanisms of the process of interest are known, the aim is at manipulating the competitive branching ratios, *i.e.*, selecting the pathways to yield desired products by optically influencing the molecular dynamics. Means to achieve the control have been developed for frequency and amplitude shaping of a pulse, to produce optimal fields in steering the wave-packet nuclear motions on and between different electronic states.^{4–9} After the first decades of pioneering work in the field, the interests now range from systems of few degrees of freedom to complex biological structures.¹⁰ With the present system we bring in an in-between contribution to the field. While the diatomic ClF molecule acts as a simple prototypical object, the crystalline rare gas surrounding complicates and adds its multidimensional solid state flavor to the analysis of the spectral observations. We have clarified the spectroscopic properties to acquire information on the ClF excited states, and used the pump–probe scheme to characterize the ultrafast dynamics in rare gas matrices.^{11,12} With a diatomic molecule, the reaction controllability is limited on photodissociation *vs.* lattice cage induced geminate recombination, if we exclude the class of mere intramolecular electronic transitions from the present control reaction concept. For concentrated samples, reactions between isolated molecules may take place *via* diffusion of the molecular fragments after dissociation. In addition, the fragments may create charge-transfer complexes with rare gas atoms.¹³

The determining property for dissociation in a cage is molecular alignment. Controlling the alignment, we can control the

photoreactions. As becomes clear from a recent review article,¹⁴ a significant body of work has been devoted to the ability of intense nonresonant laser fields to align molecules. The alignment is, classically speaking, due to laser-induced anisotropic polarization, and the torque thus experienced by the molecule. To the best of our knowledge, no successful experiments nor theoretical investigations have been carried out for molecular alignment with ultrashort pulses in the solid state. To move in this direction, we quantify computationally the conditions for our candidate system, ClF embedded in Ar or Kr solids, and explore the possibility for the experiments. The well-studied pump–probe scheme is discussed as a convenient and time-dependent detection method for the alignment effect.

Nonadiabatic molecular dynamics simulation methods including surface hopping and quantum analysis of the population changes in the potentials have been developed^{15,16} and utilized for rare-gas embedded homonuclear halogen molecules such as I₂, Cl₂, and F₂.^{17–19} Interhalogens introduce a complication due to symmetry breaking. Therefore, explicit theoretical work on ClF dynamics has been performed only with a low-dimensional model (quantum mechanical) and for a rather short simulation time.²⁰ We have a twofold goal in the present study, namely aiming at getting insight into the existing experimental observations on dissociation probability, energy relaxation and depolarization, and adding the aspect of control into these processes *via* molecular prealignment. Classical molecular dynamics is a valuable tool for a first-stage investigation of a system with high complexity, here imposed to the molecule by the solid phase surroundings. Prior to high-level quantum evaluation of, for example, the rotational or vibrational coordinates of the molecule, by solving the time-dependent Schrödinger equation, it is of key importance to know the proper conditions. With this guide, reduced-dimensionality approaches^{21–25} necessary for quantum description in large systems can be used. Here, we present a classical mechanics description to calculate observables of the ground and excited state ClF molecule in Ar and Kr solids, dictated by the input potentials for atom-atom interactions and the adopted computational method. Interpretation of

[†] Present address: Max-Born-Institute, Max-Born-Straße 2A, D-12489 Berlin, Germany.

experimental results in the light of the present outcome is postponed to the accompanying article,²⁶ where an additional quantum-mechanical study on librational states is carried out.

The paper is organized as follows. First, we describe the computational methodology in attaining the various aspects of the study in Section II. We start the simulations with trajectories on the CIF ground state potential and extract properties such as preferential orientation and its temperature dependence from the trajectories in Section III A. We proceed to executing the strong-field alignment scheme on the ground state and discuss the parameters involved in the interplay of potential barrier and induced rotation in Section III B. Next, we consider the excitations above the gas-phase dissociation limit and discuss the dissociation probability dictated by thermal distribution of molecular orientation, and characterize the energy relaxation, bond-rotation, and round-trip times for the recombining trajectories in Section III C. Finally, we add the aspect of control to the dissociation *vs.* recombination using an alignment-pump scheme to specifically distinguish between different initial conditions before the excitation in Section III D. Concluding remarks are given in the Section IV, where we address the key features observed which have to be further analyzed and compared to experiments in the continuation.²⁶

II. Computational method

The simulation cube is constructed from the rare gas atom coordinates for $4N^3$ lattice sites in an fcc crystal structure. The size of the cube is thus determined by N for which we use 3–5 (108–500 sites) depending on the case under study. The impurity molecule CIF is introduced in a central position of the cube in a single substitutional manner, having its center of mass fixed at the lattice site. Periodic boundary conditions are applied in determining the interaction potentials, forces, and atomic movement as described below.

A. Potential energy surfaces

The interaction between rare gas atoms is handled by a pairwise summation over the isotropic potentials. We use a Buckingham-type function of form

$$V(r) = Ae^{-Br} - C/r^6 - D/r^8, \quad (2.1)$$

where $A = 10\,323.2$ eV, $B = 3.59345$ Å^{−1}, $C = 30.0806$ eV Å⁶, and $D = 626.0$ eV Å⁸ for Ar–Ar pairs, whereas for Kr–Kr we apply $A = 10\,635.3$ eV, $B = 3.26046$ Å^{−1}, $C = 53.6847$ eV Å⁶, and $D = 1780.38$ eV Å⁸. These parameters reproduce accurately the pair interaction, derived (Hartree–Fock-dispersion model HFD-B) from the experimental scattering data by Aziz and Slaman,²⁷ within the energy scale of interest here (up to at least 1 eV).

For the relevant electronic states of the CIF impurity molecule in this study, X ¹Σ₀⁺, B ³Π₀, and ¹Π₁, the potentials are obtained from the *ab initio* results of Alekseyev *et al.*²⁸ and implemented in the Morse potential form for the first two of the states, whereas the repulsive ¹Π₁ is represented by eqn. (2.1) with $A = 89\,046.8$ eV, $B = 7.56591$ Å^{−1}, $C = -10.4983$ eV Å⁶, and $D = -49.837$ eV Å⁸. The parameters for the Morse function,

$$V(r) = D_e[e^{2\beta(1-r/r_e)} - 2e^{\beta(1-r/r_e)}], \quad (2.2)$$

are $D_e = 2.6$ eV, $r_e = 1.64$ Å, and $\beta = 4.3$ for the X ¹Σ₀⁺ state, and $D_e = 0.265$ eV, $r_e = 2.0099$ Å, and $\beta = 6.0066$ for the B ³Π₀ state.

The anisotropic interaction of the impurity halogen atoms with rare gas atoms is taken into account by a reduced diatomics-in-molecules (DIM) scheme,¹⁵ where the interaction

matrix is projected onto a particular molecular state, yielding

$$V(r) = \sum_{\text{Cl,F}} \sum_{i=1}^{N_{\text{Rg}}} (V_0(r_i) + F V_2(r_i)(3 \cos^2 \gamma_i - 1)), \quad (2.3)$$

where the prefactor corresponds to $F = 1/10$ for the singlet states and $F = 1/20$ for the B ³Π₀ state. The isotropic part of the function, $V_0 = (V_\Sigma + 2V_\Pi)/3$, and the anisotropic part, $V_2 = 5(V_\Sigma - V_\Pi)/3$, contain the collinear (V_Σ) and perpendicular (V_Π) interaction terms between the halogen p-orbital hole and the spherical rare gas electron density. As a result of the state-specific diagonalization, the parameter γ entering is defined as an angle between the current molecular axis and the line connecting a halogen–Rg pair. The interaction parameters along with the piecewise functions are given in the molecular beam studies of Aquilanti *et al.*^{29,30} and applied here in the same functional model. A cutoff distance of 12 Å is used in all the above evaluations without further long-distance corrections.

Prior to discussion of the photodynamics stage, we check the local energetics around the impurity molecule. We produce the angular dependence of the potentials in a fixed lattice with perfect or dynamically thermalized rare gas atom positions, and apply steepest descent geometry optimization (without a line search). In this way we obtain insight into preferred orientation and lattice cage structure in a static case. The definition of coordinates, angles, and so-called cage windows relevant to this study is presented in Fig. 1, where we also label three of the nearest neighbour atoms by A, A' and B for comparison to other figures.

B. Dynamics

The dynamics simulation is initialized by generating the Rg atom momenta randomly with a distribution according to a given temperature ($v_{\text{rms}} = \sqrt{3k_B T/m}$) and scaling the total cell momentum to zero. The CIF bond length is initially equal to the equilibrium distance, and after thermalization it is set to the classical turning point in order to simulate the ground state zero-point vibration amplitude. The initial orientation of the

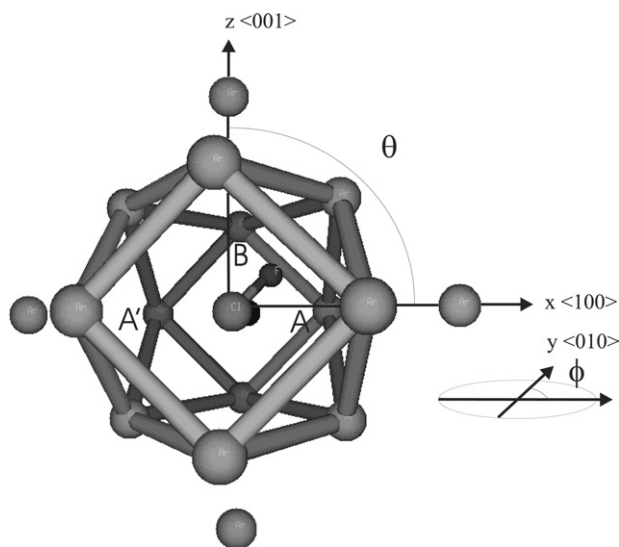


Fig. 1 The fcc lattice cage surrounding a single substitutional CIF molecule. The 12 nearest neighbour Rg atoms and five next-nearest atoms are shown, the point of view being that of the sixth second nearest atom at (010). The nearest neighbours comprise six four-atom windows and eight triatom windows for cage exit. The molecule is oriented towards <111> direction in the picture ($\theta = 54.7^\circ$, $\phi = 45.0^\circ$). The letters A and A' label two of the nearest neighbours in the *xy*-plane ($\theta = 90^\circ$) and B is one of the atoms comprising the tetraatomic window to which the molecule is oriented in most cases of the following simulations.

molecule in Ar is $\langle 001 \rangle$, i.e., along z with $\theta = 0^\circ$ always, according to the preferred situation found in Section III A. For Kr we use for the same reason $\theta, \phi = 90^\circ, 45^\circ$ when excited with 387 nm pump light (cf. Section II D), whereas $\theta = 0^\circ$ is again used for the 308 nm excitation case to allow comparison.

The classical equations of motion are integrated numerically according to the velocity Verlet algorithm^{31,32} with 0.25 fs time steps, where the forces are obtained from analytic potential gradients due to the simple reduced DIM formalism. We run the simulations at the 5 K and 19 K temperatures corresponding to the experiments.^{11,12} In addition, we apply the scaled temperature approach of Bergsma *et al.*³³ designed to account for quantum zero-point motion by

$$T' = \frac{\theta_D}{2} \left(\tanh \left(\frac{\theta_D}{2T} \right) \right)^{-1}, \quad (2.4)$$

which gives $T' = 46$ K and 36 K for Ar (Debye temperature $\theta_D = 92$ K) and Kr ($\theta_D = 72$ K), respectively.³⁴

During the early stage of the simulation, the system is subject to thermalization by a continuous velocity rescaling (pseudo- NVT Berendsen method),³⁵ which forces the system towards a desired temperature. In addition, we deterministically rescale the simulation cell volume after each step, thus forcing the system to zero pressure (NPT). After the thermostat–barostat stage of *ca.* 5 ps, the trajectory simulation strictly obeys microcanonical (NVE) ensemble conditions during the ground and excited state propagations.

Several observables are recorded during the simulation runs. For the system control, we monitor the total energy, temperature and a possible strain computed from the virial. The molecular properties followed are the CIF bond-length, momentum, center-of-mass motion, molecular angle, and distances to nearest Rg atoms. We store all the atom coordinates and calculate radial distribution functions during the different simulation stages.

C. Alignment

The effect of an intense nonresonant laser field to produce alignment is due to the interaction between electric field vector of radiation and the anisotropic polarizability of the molecule.³⁶ The effective potential imposed on the diatomic molecule, entering the quantum mechanical Hamiltonian expression,

$$U(\Theta, t) = \left(\frac{E_0^2}{4} (4\pi\Delta\alpha) \sin^2 \Theta \right) g(t), \quad (2.5)$$

has as parameters the field strength E_0 , the anisotropy of polarizability tensor $\Delta\alpha$, the angle Θ between the field polarization and molecular axis, and the pulse profile for which we use

$$g(t) = e^{-\ln(2)(t-t_0)^2/(\tau/2)^2}. \quad (2.6)$$

The actual implementation in our classical approach consists of imposing external gradients to the molecule, calculated from the above potential, eqn. (2.5), with

$$\nabla_q U = \partial U / \partial \Theta \cdot \partial \Theta / \partial q, \quad q = x, y, z$$

depending on the chosen field polarization direction, and thus actively forcing the molecule towards parallel alignment. The experimental conditions set limits to the applicability of this scheme. For example, the damage threshold of the Ar crystal is at $I = 0.8 \times 10^{12}$ W cm⁻² intensity,²⁶ giving an upper bound to the field strength via $E_0^2 = 2I/c\epsilon_r$, the relative susceptibility ϵ_r being 1.65 in this case. With $\Delta\alpha = 1.32$ Å³ for CIF,³⁷ the peak height of only *ca.* 7 cm⁻¹ for U is reached, interpreted as lowering of the rotational barrier up to this number. We use a constant $\tau = 160$ fs pulse length and vary the field

strength and polarization direction in the simulations. Note that we have neglected the $-E_0^2\alpha_{||}/4$ term in eqn. (2.5) since it gives no effect in the present gradient approach.

With ultrashort pulses the mechanism of strong-field alignment is nonadiabatic, so that rotational wave packets are excited and a delayed post-pulse alignment follows with possible recurrences for free molecules.³⁸ Our classical treatment with gradients giving a kick towards the parallel orientation mimics the delay on which the process occurs, with an additional restriction imposed by the hindering lattice cage.

D. Pump excitation scheme

The excitations $B^3\Pi_0 \leftarrow X^1\Sigma_0^+$ and $^1\Pi_1 \leftarrow X^1\Sigma_0^+$ are pumped in the experiments with laser pulses at 387 nm ($\tau = 150$ fs) and 308 nm ($\tau = 50$ fs), respectively.¹¹ We use the difference potential ΔV between the ground state and a final state as a resonance condition for excitation (sudden change of the CIF potential) defining r_{pump} bond length by $\Delta V(r_{\text{pump}}) - \hbar\omega_{\text{pump}} = 0$. We apply a Gaussian probability function $\exp(-(r - r_{\text{pump}})/w)^2)$ around this energy, the range w given by the spectral width of the laser pulse. Whenever a trajectory passes through this pump window range the probability $[0, 1]$ is compared to a generated random number between $[0.5, 1.5]$. If the probability value is higher than the random number, excitation takes place. This choice of the random number range keeps the excitation probability low, and produces a distribution of momenta and CIF bond lengths for the moment of excitation since the excitation can happen at inward or outward bond stretch. Therefore, the simulation artificially accounts for the finite band width of the ultrashort laser pulse. The different excitation times thus created are rescaled to a common $t = 0$ for presentation of the excited state trajectories.

Due to the high-energy nature of the process, the largest simulation cube size ($N = 5$) is used, in order to avoid the possible artifacts produced by the periodic boundaries and shock waves generated.³⁹ Even with this precaution in mind, the simulations can be expected, in this respect, to be reliable only for the first picosecond after the excitation. Another, and more severe, limitation is, obviously, the neglect of coupling and nonadiabatic transitions to the rest of the valence states. Moreover, the identity of a molecular state at long interatomic distances is not assignable to a specific $^M A_\Omega$ state according to Hund's case (a).

In the case of 387 nm excitation, we however assume that the molecule stays in its B state. We record the single-potential CIF trajectory for the later²⁶ construction of a pump–probe spectrum and its experimental comparison. The energy relaxation of both the impurity molecule and the kinetically-excited host atoms is followed. Furthermore, we show a short-time RDF (radial distribution function) to visualize the atomic movement during the first vibrational excursions. The change in the molecular axis direction after photoexcitation is the parameter to be discussed in connection with the experimental depolarization time.²⁶ To keep the nomenclature consistent, we assign reorientations of greater than 60° in simulations to depolarization.

For the excitation to the higher $^1\Pi_1$ state, we are mainly interested in the sudden dissociation probability. From our experiments⁴⁰ it is known that collision-induced spin flip occurs in a sub-picosecond time scale as the singlet and triplet potential surfaces approach degeneracy. For this reason, we change the molecular potential from $^1\Pi_1$ to that of the $B^3\Pi_0$ state at 100 fs after the excitation. Moreover, the halogen atom–rare gas interactions are treated isotropically for both excited states in this case, in order to at least partially account for orbital reorientations¹⁹ at long molecular distances (merely allowing free rotation, no orbital locking). In this way an abrupt dip in the potential energy is also avoided, while there

is a small difference in the anisotropic part of the potentials due to the F -factor in eqn. (2.3).

III. Results and discussion

A. Ground state dynamics

1. **Ar matrix.** In this section we proceed in five steps to describe the energetics and dynamics of the trapped impurity molecule and the surrounding lattice atoms:

(a) In the first stage of the simulations we determine the temperature dependence of the lattice constant by requiring the pressure to remain zero.

(b) Then, for the corresponding simulation cube sizes, we determine the potential barriers $V(\theta, \phi)$ by rotating the molecule in a perfect static lattice. The molecular bond length is kept at the equilibrium distance r_e .

(c) We repeat the previous procedure for a thermalized lattice to obtain $V(\theta, \phi)$ in a locally adjusted surrounding, and take an average over the trajectories. To follow the orientational dynamics, we establish a classical representation of a rotational wavefunction, *i.e.* a histogram of $\theta(t)$ and $\phi(t)$ values which we define as a density $\rho(\theta, \phi)$, in the following way: We record the molecular angle information during the ground state propagations and arrange the result to angular distribution $\rho(\theta, \phi)$. The angle data is collected from the latter 4 ps of the two 5 ps simulation stages, *i.e.*, during thermalization and NVE ground state propagation.

(d) The second step (b) is repeated also for a geometry-optimized lattice (*i.e.* gradient search of energy minimum at 0 K, for all degrees of freedom) and the resulting $V(\theta, \phi)$ is compared to the above dynamical case (c).

(e) Finally, we consider the bond stretch of the molecule and report the results as a potential $V(r_{\text{CIF}}, \gamma)$, where the molecular angle γ labels the orientation to either two of the cage windows, both in static and dynamically evolved lattices.

The first stage of the simulation (a) comprising the weak-coupling isothermal–isobaric method leads to the following zero-pressure conditions: At 5 K, the average lattice constant (LC) over the trajectories is at (5.2238 ± 0.0004) Å with scaled density $\rho^* = 1.0597 \pm 0.0003$. For 19 K and 46 K the values become (5.2474 ± 0.0011) Å, 1.0456 ± 0.0006 and (5.301 ± 0.003) Å, 1.014 ± 0.002 , respectively. The dimensionless variable ρ^* is defined by $\rho^* \equiv \rho \sigma_0^3$, where σ_0 is the Ar–Ar distance (3.35 Å) at which the potential crosses the energy zero. With the present gas-phase derived Aziz–Slaman²⁷ Ar–Ar potential, $\rho^* = 1$ corresponds to the pair-potential guided value of the lattice constant of 5.3125 Å, close to the 0 K bulk value 5.311 Å.⁴¹ The simulation cube thus shrinks from the initial $\rho^* = 1$ structure. With the CIF impurity the reduction in volume corresponds to $2\text{--}700 \times 10^{-6}$ Å³ for all the above temperatures, and the total potential energy of the system decreases also with shortening LC.

We show how the lattice size due to the three applied temperatures affects the rotational potential energy barrier in Fig. 2. Here, in the scheme (b), the lattice atoms are fixed with $LC(T)$ and due to the O_h symmetry only one octant is shown. The molecular center of mass is placed at the substitutional site with the equilibrium ground-state bond distance. The potential energy plots show the maxima at the nearest neighbour lattice atom directions, $\langle 110 \rangle$, whereas the $\langle 100 \rangle$ global minima are in competition with the triatomic windows $\langle 111 \rangle$ when temperature (and lattice constant) is increased, eventually yielding a low saddle point at a tetraatomic window (see Table 1).

The local interaction symmetry and the lattice structure around the impurity are obviously different from the bulk, and moreover, are time dependent. Therefore, we show also a time-dependent ensemble-averaged potential at 5 K in upper panel of Fig. 3. Here in the (c) stage we have taken snapshots of Rg atom positions after the thermalization and calculated

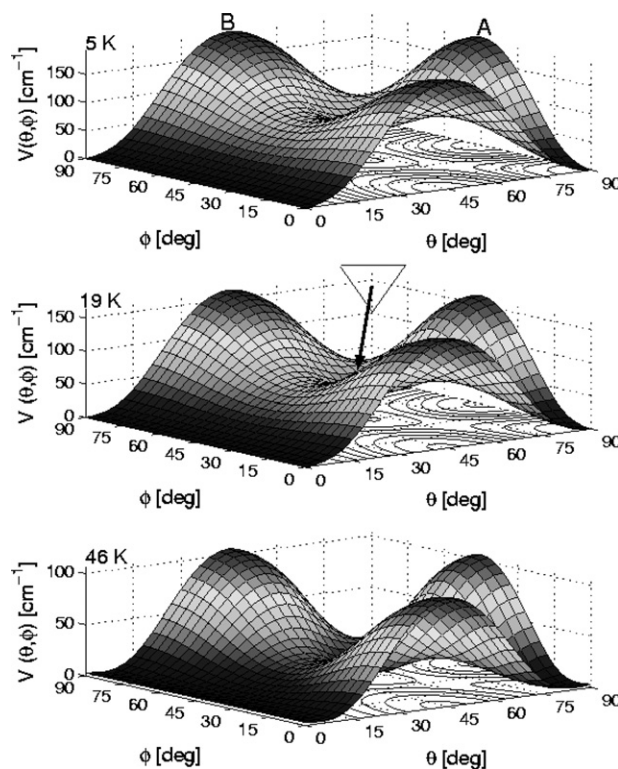


Fig. 2 The rotational potential energy barriers for CIF in Ar at zero pressure conditions from 5 K, 19 K, and 46 K temperatures. Directions towards nearest neighbour maxima at A and B and the triangular window local minima are indicated in the picture. Static O_h structure is assumed for local symmetry.

the rotational potential from another set of 50 trajectories with $N = 4$. In all these thermalized trajectories the molecular axis is found to precess around the $\langle 001 \rangle$ direction with *ca.* $\theta = 16^\circ$ librational angle (see Fig. 4), *i.e.* an F atom pointing in the original direction towards the positive z -axis. It can be seen in the Fig. 3 that the tetraatomic window retains its preference for molecular orientation, however, the nearest neighbour atoms are no longer equidistant from the interaction centre. Also, the other tetraatomic windows not occupying the molecular axis are higher in energy than the one to which the molecule points during thermalization. This is largely due to the fact that the Ar atom in $\langle 001 \rangle$ direction is pulled towards F in the equilibrium coordination. This semi-static picture does not tell, however, what happens energetically during the rotational or reorientational time scale, when lattice atoms adjust their positions accordingly. As observed from the angular distributions $\rho(\theta, \phi)$ presented in Fig. 4, the orientation is no longer locked at higher temperatures. In the 19 K case occasional reorientations take place, whereas at 46 K the molecular

Table 1 Collection of rotational energy barriers in cm^{-1} for triatomic (3W) and tetraatomic (4W) windows, the nearest neighbour orientations (nn), and the saddle points between windows ($3 \leftrightarrow 4S$) or other minima for CIF in Ar and Kr. The scaled temperature T' is defined in eqn. (2.4)

T/K	Ar				Kr			
	3W	4W	nn	$3 \leftrightarrow 4S$	3W	4W	nn	$nn \leftrightarrow nnS$
5	57	0	193	88	168	286	0	139
19	38	0	165	65	171	286	0	144
T'	5	3	106	24	172	281	0	146
Time-dependent averages								
5	104	34	18	—	105	292	0	76

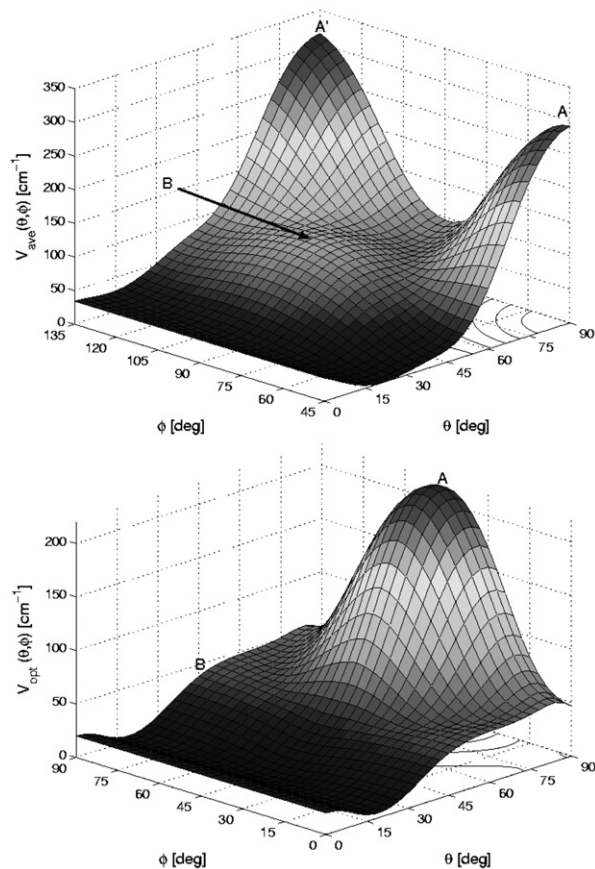


Fig. 3 Upper panel, stage (c) in the text: Averaged rotational potential for CIF in Ar at 5 K after the thermalization stage. The calculated angular range covers one octant of the sphere and shows that nearest neighbours in the xy -plane (here at $[\theta, \phi] = [90^\circ, 45^\circ]$ A, and $[90^\circ, 135^\circ]$ A') are energetically different from $[45^\circ, 90^\circ]$ B, as are the two tetraatomic windows ($\theta = 0$ direction of CIF, and $[\theta, \phi] = [90^\circ, 90^\circ]$ perpendicular to CIF) in the picture. Lower panel, stage (d): Rotational potential after geometry optimization. Note the different ϕ -range.

angle distributes with broad transitions between the tetraatomic windows. In this high temperature case, for more complete mapping of the trajectories into $\rho(\theta, \phi)$, longer simulation times are necessary for the ergodicity condition. The (2×4) ps data accumulation proves sufficient for the upper hemisphere $\theta = 0^\circ$ – 90° . The sampling obtained is biased for the initial conditions due to the limited time, however, it shows the transition pathways avoiding the triatomic windows and provides a direct insight into the time-dependent potentials that maintain the energetic preference for square window orientations. Comparing now Figs. 3 and 4 we find that although the triatomic window is lower in energy after thermalization,

the preferred path to another tetraatomic window passes over the barrier indicated by atom B in the figures, which finally gives a rather complete picture of energy relations of the reorientational dynamics.

The effective rotational barrier estimated as $ca. 90 \text{ cm}^{-1}$ in the static case thus experiences drastic changes as the thermal movement of the lattice atoms drives the molecule into (pseudo)-rotation. This is a combined effect of random thermal collisions and lowering of the differences between tri- and tetraatomic windows due to the pressure scaling. It is noted, however, that the thermal excitations play a major role since with constant lattice size at $\rho^* = 1$ the increasing temperature had a similar effect in test simulations.

We obtain further insight in stage (d) by checking whether our picture of preferential orientations is coincident with geometry optimization results for the lowest temperature considered here. In this LC(5 K) case, the CIF center-of-mass (COM) moves upwards along the z -coordinate by $ca. 0.2 \text{ \AA}$ after placing the molecule at the substitutional site with $\langle 001 \rangle$ orientation. If only the lattice atoms are allowed to move in optimization, the most distinct effect is that the nearest neighbours constituting the tetraatomic window next to Cl atom are pushed outwards. It is observed by combined thermalized potential calculations and geometry optimization routines that COM motion plays a major role in displacing the center of interaction of static lattice from the molecular centre. For the higher temperatures (*i.e.* looser trapping sites) the comparison is not so straightforward to make, since due to the enhanced thermal motions also movement in other COM coordinates takes place; nevertheless, the general aspect of the local structure adjusting itself to more or less cylindrical symmetry is still present. The two panels in Fig. 3 show a qualitatively similar result for the barrier with respect to orientation, however the heights of the saddle points and maxima are somewhat more pronounced in the dynamical case.

Additional information to the above orientational features comes in stage (e) from the vibrational coordinate of the CIF molecule that samples the barriers for cage exit. The energy dependence of the fragment orbital orientation with respect to a triatomic window plane, parallel or perpendicular, was studied before for F in Ar and Kr, and it showed $ca. 1 \text{ eV}$ difference due to the anisotropic repulsive interaction.⁴² In that case, the p-orbital basis DIM yields an energy difference of $9V_2(d/\sqrt{3})/10 = 0.8 \text{ eV}$ for F fragment in the centre of a triatomic window, d being the nearest neighbour lattice distance. This energy difference is concluded to provide a torque aligning the fragment orbital as the projectile reaches the cage wall. Moreover, it was found that in the window area the actual minimum for parallel orientation is between the triangle atoms with additional in-plane locking of the orbital towards the nearest atoms ($V_{\parallel} = 2V_{\Sigma}(d/2) + V_{\Pi}(d\sqrt{3}/2)$, leading to the $ca. 1 \text{ eV}$ difference). In other words, change of the molecular electronic state is necessary for the dissociation to take place.

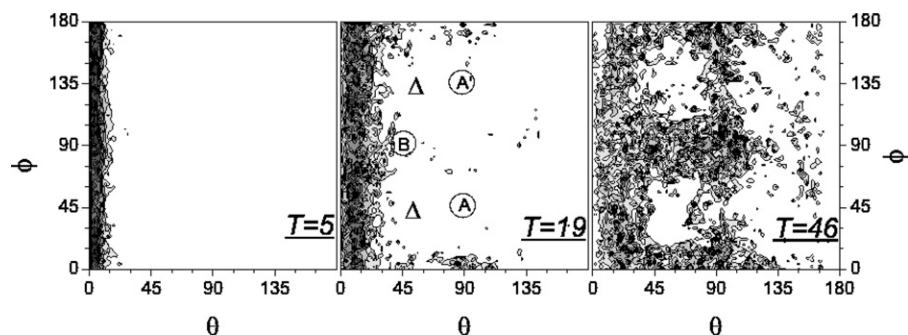


Fig. 4 The density contour plot of the molecular angle as a classical representation of the rotational wavefunction $\rho(\theta, \phi)$ evolved for 4 ps by MD simulation. Nearest neighbour A, A', and B locations and two of the triangular windows Δ are indicated in the middle panel ($T = 19 \text{ K}$) to guide the eye. The maximum amplitude is scaled to unity in all the plots.

This is in accord with recent nonadiabatic MD simulations for F_2 .¹⁹

The above consideration was for a single F atom. We treat the case of a molecule CIF and an appropriate molecular-state specific projection is applied here. In this case the difference between the lower adiabatic valence states, $V(A' \ ^3\Pi_2) = V(A \ ^3\Pi_1) = V_0(r)$ and $B \ ^3\Pi_0$ or $^1\Pi_1$, is only $FV_2(r)$ (see eqn. (2.3)), since the method reflects the short-range electronic cloud properties of two singly occupied molecular orbitals. In the present case, upon the single-electron excitation ($\pi^* \rightarrow \sigma^*$) the more electronegative F atom is left with a localized orbital of σ^* nature at $r > 2.1 \text{ \AA}$,²⁸ meaning that on dissociation the orbital is parallel to the direction of motion, that is, perpendicular to the window plane. The present simulation does not include surface hopping; however, it is expected to be of little importance for the analysis of time behavior in the recombining trajectories because of the small value of FV_2 in this region.

Fig. 5 gives an idea of the energetics by showing potential energy cuts $V(r_{\text{CIF}}, \gamma)$ for the stretching molecule in two directions. Here, we first show a case (right panel) where the Cl atom is fixed at the substitutional position and F moves through the tri- or tetraatomic window. Then we fix the COM to the substitutional position (left panel) and move both atoms along the two directions. Finally we repeat the latter for thermalized lattices in 50 B-state trajectories showing the effect of a relaxed cage structure on the barriers. The lattice size corresponds to the 5 K case ($d = 3.69 \text{ \AA}$). The energy is scaled equally for the curves so that the case where the molecule points at tetraatomic window with Cl fixed at substitutional position has the ground state minimum value -2.6 eV . The energy difference of the states, due to the anisotropy factor F , is seen in the separation of the circles ($B \ ^3\Pi_0$ state) from the solid lines ($X \ ^1\Sigma_0, \ ^1\Pi_1$) in the right panel. As discussed above, the difference near the cage atom is less pronounced than in the F atom only case.⁴² The time-dependent barriers show the effect of locally adjusting lattice structure. For the tetraatomic exit, the barrier wall is lowered, thus allowing for longer bond stretches after the 0.6–1.4 eV of excess energy is transferred to the molecule on the 387–308 nm excitations. Oppositely, the $\langle 111 \rangle$ direction is more repulsive in the relaxed lattice. These curves may be compared to a recent reduced dimensionality approach where potential energy surfaces were calculated for a fixed Ar lattice, allowing the CIF COM to move during the bond stretch in the $\langle 111 \rangle$ direction.²⁰

2. Kr matrix. The argon lattice results given above differ qualitatively from the Kr case. The rare gas-halogen pair

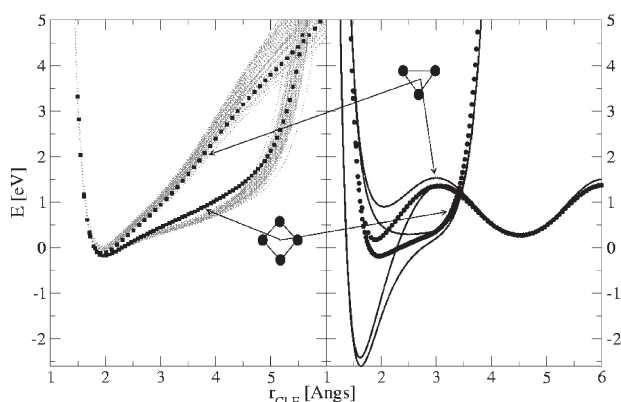


Fig. 5 Left: Potential energy barriers for CIF bond stretch into the two Ar window directions. The curves with square symbols represent the static lattice for fixed COM and the swarm of dotted lines around them are for the relaxed 5 K lattices. Right: The other two sets of lines correspond to fixed Cl and moving of F atom only, with solid lines for the singlet states and circular symbols for the triplet B.

interaction potentials are more attractive for Kr, and the trapping site is looser due to the larger lattice constant. Starting the simulations with scaled density $\rho^* = 1$ conditions, the lattice constant shrinks due to the zero-pressure constraint to $(5.5716 \pm 0.0004) \text{ \AA}$, $(5.5893 \pm 0.0011) \text{ \AA}$, and $(5.613 \pm 0.002) \text{ \AA}$ at 5 K, 19 K, and 36 K, respectively, below the 0 K bulk Kr value of 5.646 \AA .⁴¹ The rotational barriers in static lattices do not show such a variation with respect to lattice size as happens in Ar. From the minimum orientation (pointing towards a nearest neighbour) to the triatomic window (a local maximum), the barrier increase is only 4 cm^{-1} from 5 K to 36 K, and the true maximum at the tetraatomic window is lowered by 5 cm^{-1} accordingly. Therefore, we show in Fig. 6 only the 5 K static case and compare to the time-dependent average potential that has a distorted symmetry. The relaxed lattice at this temperature shows again an enlarged minimum–maximum difference. The local maximum in the $\langle 111 \rangle$ direction ($[\theta, \phi] = [55^\circ, 45^\circ]$) is however reduced by *ca.* 65 cm^{-1} from the static 168 cm^{-1} value. The other triatomic windows gain potential energy and the preferred pathway for the reorientational dynamics adopts an x-shaped form in the angular plane, utilizing saddle points around the triatomic windows.

The temperature effect on the molecular angle distribution is clearly present in Fig. 7 where we show the orientational density obtained by mapping the trajectory dynamics into $\rho(\theta, \phi)$. The rotational density is strictly localized at 5 K, but 19 K is already sufficient to promote barrier crossings. The density is seen to spread from the initial distribution and occupy the other nearest neighbour directions, filling the wells in the potential (Fig. 6). The broadening occurs *via* the saddle points and, as already discussed above, the triatomic window

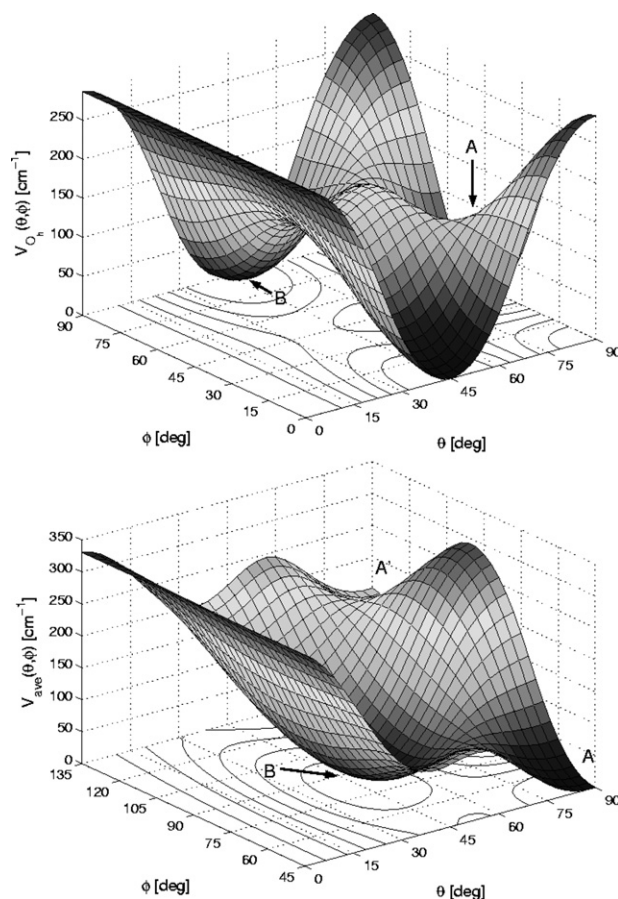


Fig. 6 Upper panel: The rotational potential energy barrier for CIF in Kr assuming O_h symmetry. Lower panel: Averaged result for 50 thermalized trajectories at 5 K, initialized from the orientation pointing to A.

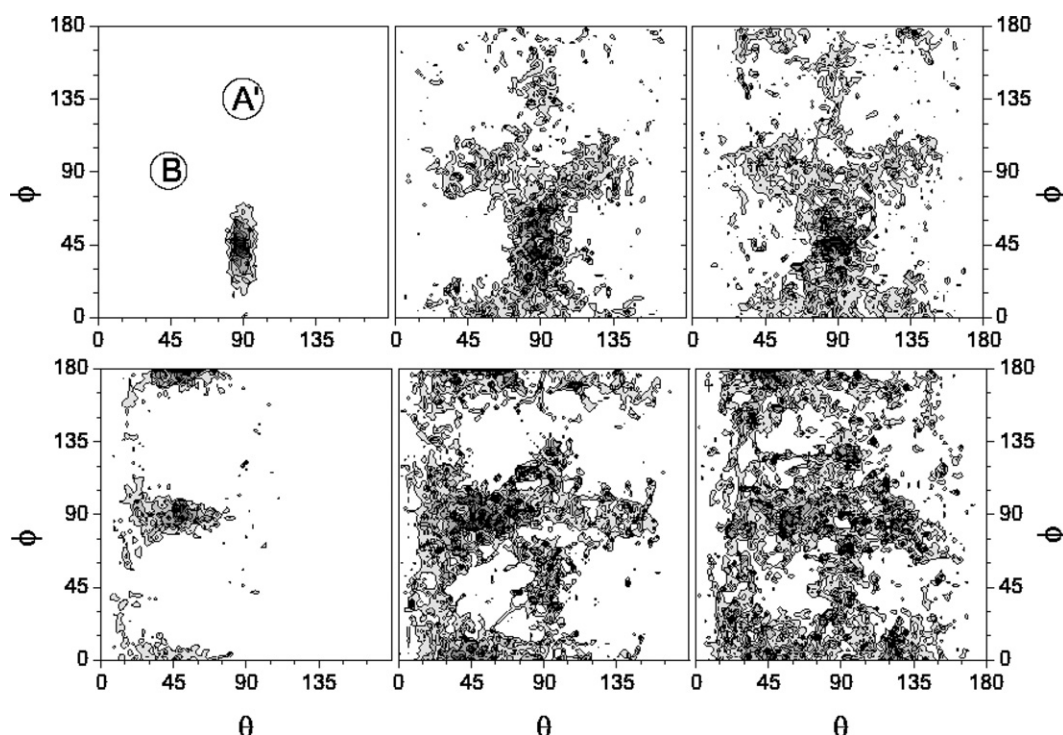


Fig. 7 The density contour plots $\rho(\theta, \phi)$ for single substitutional CIF molecule in Kr matrix collected from 4 ps MD propagation. Amplitude scaled to unity. Upper row: Initial orientation, the density at 5 K, is towards nearest neighbour A of Fig. 1. Two other neighbours are indicated in the upper left panel by A' and B. Lower row: Initial orientation set to tetraatomic window, $\theta = 0^\circ$. Temperatures from left to right: 5, 19, and 36 K.

directions are strictly avoided. Rather surprisingly, though, there is considerable population in the tetraatomic windows, implying that they are more flexible for distortions than the other window. Already at 5 K the libration has a larger amplitude in the equatorial plane. Starting the simulation from the same orientation as in the Ar case, *i.e.* from the static maximum $\theta = 0^\circ$ (lower panel in Fig. 7), $\rho(\theta, \phi)$ shows quick orientational relaxation at 5 K and depicts the symmetry properties of the lattice.

B. Ground state alignment

In order to make the alignment experimentally visible, one choice is to distinguish between recombination and alignment-induced dissociation probabilities. Another way is to rely on the recombining molecules and apply a polarization-dependent pump-probe scheme to differentiate the possible alignment effect. In this Section, we study the general possibility to control the alignment. The above reported rotational potential barriers give rise to severe obstacles with respect to free molecule case and put a drastic demand on the field intensity. First, we characterize the field strength requirement for continuous-wave alignment, and then apply it to the triatomic window direction in Ar and Kr at 5 K. This direction is chosen because it is avoided in both matrices with field-free conditions as seen from the contour plots of the rotational density $\rho(\theta, \phi)$ above. We collect the representative barrier height values for a quick reference of the energetics in Table 1.

A strict alignment into the $\langle 111 \rangle$ direction, and keeping this orientation steady in an adiabatic limit, requires extremely high field strengths, for the external force goes to zero once the molecule is parallel to the field polarization and the orientation is labile around a maximum of the lattice potential. Therefore, the molecular orientation is found merely to oscillate around the desired direction with constant field strength (square pulse), provided that the applied intensity is high enough (roughly, $I > 5 \times 10^{13} \text{ W cm}^{-2} \cong 420 \text{ cm}^{-1}$ external peak energy).

The ultrashort alignment field produces a transient post-pulse orientation in the desired $\langle 111 \rangle$ direction, crossing the triatomic window and continuing to a minimum orientation. Therefore, the time delay between alignment and pump pulses must be very short to catch the proper angular distribution. In Ar, because the preferred orientation is at the tetraatomic window, the orientation after it passes the triatomic window quickly points to the nearest neighbour, and if the pump pulse comes too late after aligning, the cage-exit probability is missed. The same happens in Kr, where after passage through the triatomic window the molecule finds itself pointing between the two atoms composing the triangle and collides upon bond stretch with a third coordination shell atom after the same pump delay.

Finally, we aim at populating the otherwise repulsive triatomic window orientation without extensive rotational excitation by applying a constant field (CW) of $I = 8 \times 10^{13} \text{ W cm}^{-2}$ for 4 ps ground state evolution and subsequently exciting with a 387 nm or 308 nm pump pulse. We repeat this for 50 trajectories with $N = 3$ and look for the recombination/dissociation results represented by the ensemble in Section III D. The continuous-wave simulation before pump excitation is favored over an abrupt orientation change in order to allow the lattice to respond to the reorientation and to obtain the physical energetics of the system. However, it has to be kept in mind that the applied pulse is two orders of magnitude too intense with respect to the damage threshold of the matrix.

C. Excited state trajectories

1. Ar matrix. The 387 nm excitation into the $B^3\Pi_0$ state, 0.6 eV above the gas phase dissociation limit, leads to recombination in all the 50 trajectories for the three temperatures utilized, as shown in the Fig. 8. In the graph, the collection of individual trajectories from the simulated ensemble represents a wave packet $P(r, t)$, obtained by binning the occurrences of $r_{\text{Cl-F}}$ into discrete time-slices, and introducing an additional Gaussian smoothing for the positions counted. No convolution

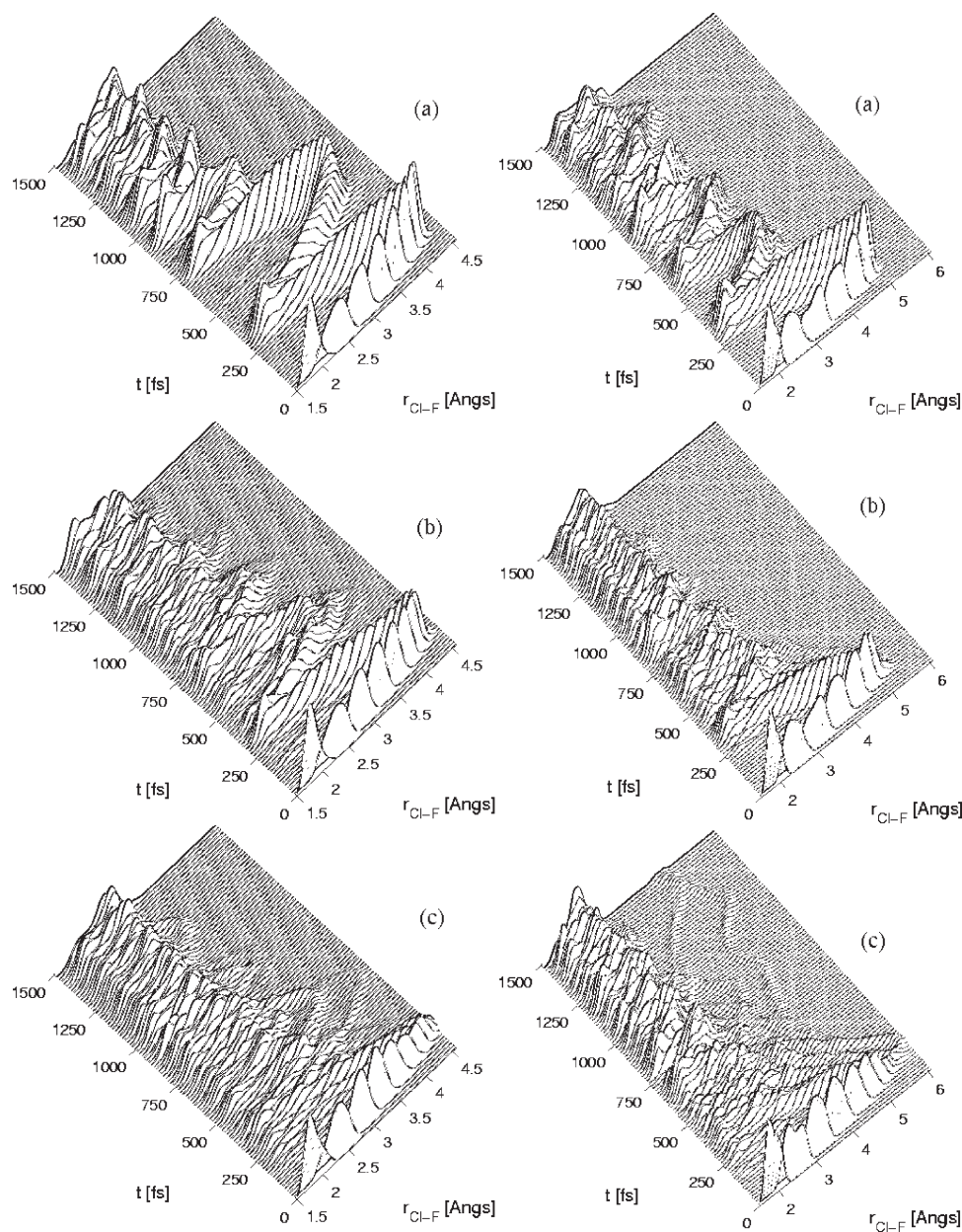


Fig. 8 Left: The interatomic distance of ClF in the $B^3\Pi_0$ state after 387 nm excitation at the three simulated temperatures in Ar matrix: (a) 5 K; (b) 19 K; (c) 46 K, presented as a classical construction of the wave packet $P(r,t)$, where classical positions are replaced by Gaussian functions with FWHM of 0.2 Å. Right: The Cl-F interatomic separation after 308 nm excitation into the $^1\Pi_1$ state, and consequent evolution of $P(r,t)$ on the $B^3\Pi_0$ state.

to account for the time dependence of the excitation is performed.

For the well-oriented 5 K case, the excitations exclusively shoot the F atom right through the middle of the tetraatomic window, opening the window and pushing the direct collisional partner at the second nearest neighbour position in a such way that also on the second excursion, the fluorine exits the cage through this window. This is evident in the distinct vibrational structure seen in the top left panel of Fig. 8, and gives the long-period limit of 330 fs for the first round trip. Averaging the 5 K trajectories we find inner turning points with 330 fs, 410 fs, and 200 fs separations, followed by three constant 160 fs oscillations, counting from time zero. The outer turning points are found with 410 fs, 320 fs, and subsequent three 160 fs time differences. At the higher temperature of 19 K, the trajectories show additional contributions from more direct collisions to the cage atoms, therefore the first round-trip times get shorter. The common factor for these shortest trajectories recombining at 160–170 fs is the excitation angle pointing close to the

nearest neighbour positions. The highest temperature case shows all the possible recombinative features that the cage symmetry induces.

The highly localized ground state $\rho(\theta, \phi)$ at the lowest applied temperature preserves the orientation of the bond also after the excitation. The molecular angle shows less than 30° change with respect to the moment of excitation within the first 1.5 ps, *i.e.*, the angular cone is maintained within the original window direction. At higher temperatures, due to the larger distribution of orientations before the excitation, more effective scattering takes place and changes the molecular angle on collisions, so that flipping to other window directions occurs.

The 308 nm excitation into the $^1\Pi_1$ state, 1.4 eV above the gas phase dissociation limit, leads to results very similar to the 387 nm case as shown in right panel of Fig. 8. With higher kinetic energy of the Cl and F fragments the elongation of the molecular bond is however enhanced, which ultimately leads to rare dissociation occurrences at the highest applied

temperature (graph (c) in the figure). From the trajectory average we extract the following time structure for 5 K: The resolvable inner turning point separations are 350 fs, 290 fs, 270 fs, and 200 fs, whereas the differences of CIF distance maxima are 390 fs, 280 fs, and 230 fs. The single direct cage-exiting trajectory at 46 K perfectly occupies the triatomic window at the moment of excitation ($\theta, \phi = 56^\circ, 43^\circ$), whereas the other exit is delayed and occurs on third oscillation with angles $\theta = 20^\circ$, $\phi = 56^\circ$, therefore finding a different route to the final trapping location for F which is the nearest interstitial site with octahedral symmetry. The two most distinctly delayed recombinations, after 1 ps, both have a slightly disoriented angle with respect to a tetraatomic window, with $\theta = 77^\circ$ and 9° . Here, the exiting F fragment samples a tight tetrahedral site which is unstable and recombination therefore follows.

The majority of the recombining trajectories show an additional feature of shorter and quicker bond stretch on second oscillation with respect to the lower energy excitation. This underlines the sensitivity of the round-trip times to the lattice window and collisional partner motions after the excitation. In both cases, the second stretch still coincides with opening of the window, and it seems that with shorter wavelength excitation the fragments lose more momentum on head-on collision with the second nearest neighbour, and the fluorine has no more energy to penetrate the window. We see from the averaged CIF kinetic energy relaxations in Fig. 9 that indeed the energy loss is larger during the high-energy collision but the molecule is left with approximately same amount of kinetic energy in both excitation cases (*ca.* 0.25 eV, slightly below the B state gas-phase dissociation). Another cause for the difference is the obviously delicate balance for metastable-like site formation, depending on the coordinates of the five kicked Ar atoms nearest to the tetraatomic window centre. This is however counter-intuitive since in the high-energy excitation the window opening due to more displaced atoms should favor the barrier lowering. The difference must therefore arise from the COM motion which is also quite different between the two cases. Since the trajectories have relaxed to the bound region of the B state, the F fragment simply does not reach the window anymore if the COM is nearly half a lattice constant away from the window centre. From the 5 K 308 nm trajectories we find that COM is located around the substitutional site when the molecule is at the inner turning point at 350 fs, whereas for the 387 nm case the COM *z*-coordinate is *ca.* 0.5 Å closer to the window, allowing the fluorine to exit. After

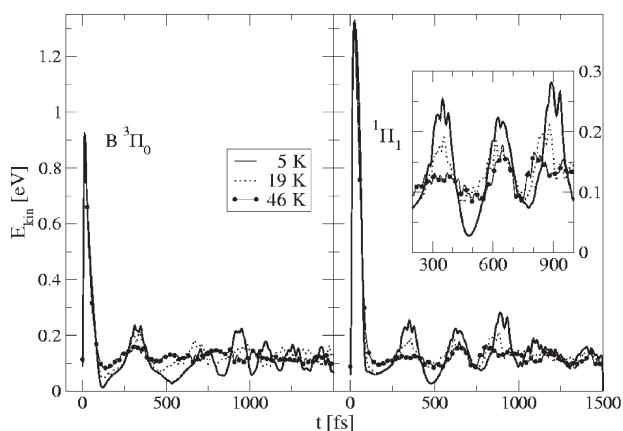


Fig. 9 The kinetic energy of CIF molecule in Ar, averaged over 50 trajectories, after excitation with 387 nm (left panel) or 308 nm (right) laser pulses. In the latter case the potential is switched to that of the B state after 100 fs. Vanishing of the oscillations at higher temperatures is contrasted in the inset. In both excitation cases the excess energy is lost during the first collision and the molecule oscillates in the bound part of the B state ($D_e = 0.265$ eV).

the second stretch, the fluorine is somewhat held in the window, and it is the Cl atom that moves mainly on recombination, therefore lifting the COM momentarily in the *z*-direction up to 1.3 Å above the substitutional position. The kinetic energy rise at 900 fs in Fig. 9 coincides with the relaxing COM motion.

To discuss the energetics of the cage exit process we show the time-dependent potential felt by the molecule after the excitations in Fig. 10. These results are from two sets of 50 trajectories with $N = 4$, all recombining, and considered free of possible periodic boundary artifacts up to 500 fs. Along the potentials, the averaged r_{CIF} trajectory is shown to guide the eye. It is immediately observed that even though the F fragment exits the first rare gas coordination shell surrounding the single substitutional lattice site, there is no particular energy minimum found for permanent trapping, as might be expected for the passage through the tetraatomic window and subsequent vigorous dislocation of the collisional partner behind the window. For example, this mechanism of saddle-point formation in the window and a local minimum behind it was found for migration of a Ag atom in the Xe matrix in $\langle 001 \rangle$ direction.⁴³ Another example studied is the dissociation of Cl₂ in Xe, proving this scenario for cage exit.^{18,44} The dip in the total potential at 150 fs after 387 nm excitation, indicated by an arrow in Fig. 10a, is only due to the lattice energy rise after opening of the window and kicking off the fifth atom, which takes place while the molecule slides down the potential. For the higher energy case two such potential dips independent of the molecule are observed at 120 fs and 220 fs (arrows), implying fast propagating perturbation within the matrix atoms. In that sense, because the recombination after window passage is not hindered by the matrix, classifying the process as a cage-exit is not well grounded. We note that averaging the results in this plot smears out the distinct oscillatory features of a single trajectory after *ca.* 200 fs.

The amount of energy transfer from molecule to matrix is most clearly seen in Fig. 11, where the potential felt by the molecule is plotted as a function of the distance r_{CIF} up to 1 ps after excitation, *i.e.*, approximately for three round-trips in the B state as indicated by the numerals. The swarm of trajectories show that, upon the loss of kinetic energy during the first collision, the dislocated window atoms leave the molecule free to relax in the B state. The energy difference, as indicated by the dotted horizontal lines in the figure, between first and

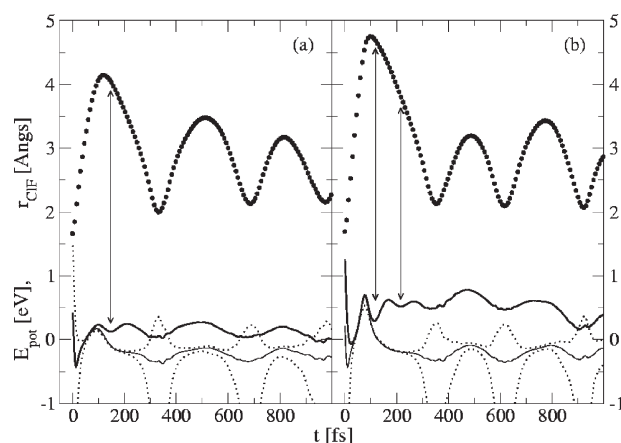


Fig. 10 The 5 K ensemble averaged results for 387 nm excitation (a) and 308 nm excitation (b). Potential surfaces experienced by the CIF molecule in Ar are plotted with dotted lines for the singlet states and solid line for the triplet B state. The thick solid line is the total potential energy including the Ar-Ar interactions for the occupied state and is scaled in the figure to match the energy experienced by the molecule in the initially populated state. The upper part of the graphs associate the averaged bond stretch r_{CIF} to the energetics.

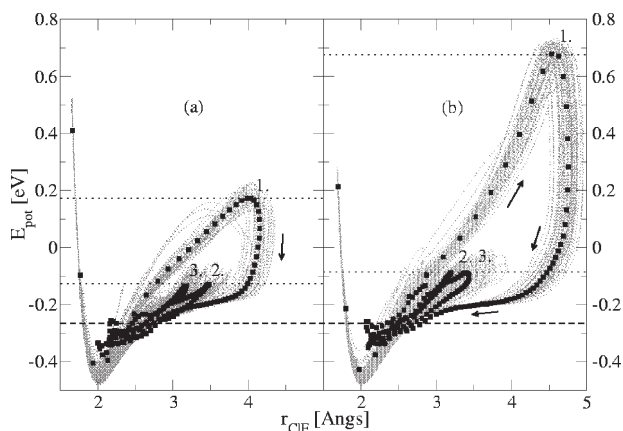


Fig. 11 Molecular potential energy in Ar as a function of interatomic distance during the first picosecond (three periods) after excitation with (a) 387 nm and (b) 308 nm pump pulses. The individual trajectories are marked by dotted curves and time-averages by square symbols. The dotted horizontal lines mark the difference in potential energy heights between first and second bond stretches. The lower dashed line locates the gas phase potential minimum for the B-state. Note that for the (b) case the $^1\Pi$ is populated for the first 100 fs although the B-state potential energy is plotted here.

second period is 0.30 eV in 387 nm case, and 0.77 eV for the 308 nm excitation. The upper line locates the average potential climbing height on the first stretch and the lower shows the second, which coincides with the third one. Obviously, most of the excess energy is transferred on the first outward trajectory, and on later oscillations the potential height reaches the same value. The different energy deposition into the lattice and the fact that the outer turning point is still moving on the third period (inwards for 387 nm, outwards for 308 nm), imply that the COM movement and lattice phonons clearly interact in a different way for the two excitation energies. The time-average in Fig. 11 shows how the two-dimensional energy-distance information loses the traceability after the first collision, and gives only an accumulating signal at the potential minimum. At the outer turning point, however, a rather well defined time structure persists for a few periods due to slower wave-packet movement in that region. The dashed line indicates the gas phase potential energy minimum of -0.265 eV for the B state. Here, we find the solvation energy for the molecule to exceed 0.15 eV, which is attainable by the relaxed lattice geometry and chiefly due to Cl–Ar interactions.

We present in Fig. 12 movements of the three most energetic Ar atoms after the pump excitation for the well-oriented 5 K case. The distance $R_{\text{Rg-COM}}$ is measured from the point where the COM was when the excitation occurred, and shows corresponding 0.2 \AA width in the trajectories. Starting from time zero, the first excited atoms belong to the tetraatomic window at 3.7 \AA , denoted by W. Soon after, the direct collisional partner at 5 \AA , C in the figure, becomes the most energetic and retains this status up to 250 fs when the excitation hops to the next shell and continues along a nearest neighbour chain (lattice diagonals) starting at *ca.* 12 \AA from the excitation centre. Comparing the time scales to the r_{CIF} trajectories it is immediately clear that the inner turning point of the molecule at 330 fs coincides with maximum opening of the window. The window breathing period is met around 800 fs and denoted by the letter B in the figure. At this time the molecular bond stretch is again hindered by the window and most energetic lattice atoms are found near the molecule. This is also evident from the lower left panel of Fig. 12 where the hump in energy, corresponding to further energy transfer from the molecule, is marked by an asterisk. We note that two time scales are superimposed in the figure, one for atoms dislocated by the Cl fragment, and the other induced by F which is better resolved.

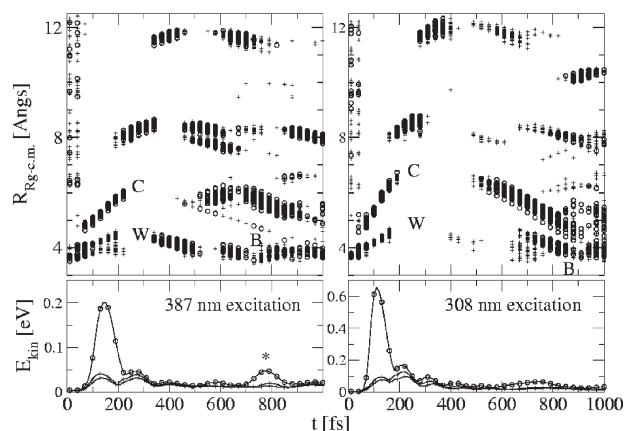


Fig. 12 Distances $R_{\text{Rg-COM}}$ from the molecular center of mass at the moment of excitation for Ar atoms with most kinetic energy, collected from 50 trajectories at 5 K. The atom with highest energy is marked with a circle and the two next highest with + labels. The labels W and C denote the tetraatomic window and direct collisional partners in the $\langle 001 \rangle$ direction, respectively, while B indicates the window breathing period. Below: The ensemble-averaged kinetic energies for the three fastest atoms.

From the dislocations with respect to time we extract velocities of $3\text{--}5 \text{ \AA ps}^{-1}$ for the window atoms and $8\text{--}14 \text{ \AA ps}^{-1}$ for the direct collisional partner with 387–308 nm excitation, respectively. The shock wave is estimated from the maximum energy hops to different shells to propagate with speeds of 30 and 37 \AA ps^{-1} in the two cases, but it is noted that due to energy redistribution it can be followed only out to 15 \AA , and is therefore not considered to affect the later dynamics near the excitation centre.

2. Kr matrix. We start the discussion of the Kr case by presenting the radial distribution functions obtained (i) from the ground state propagation, (ii) during the first 500 fs (387 nm) or 100 fs (308 nm) after electronic excitations, and (iii) during the period 0.5–2.5 ps or 0.1–1.5 ps in the B-state in Fig. 13, where argon results are also shown. The effect of molecular fragment collisions on the nearest neighbours and subsequent progression of the kinetic excitation to next shells is seen in broadening of the peaks, although not so clearly as in Fig. 12. For example, the highly dislocated direct collisional

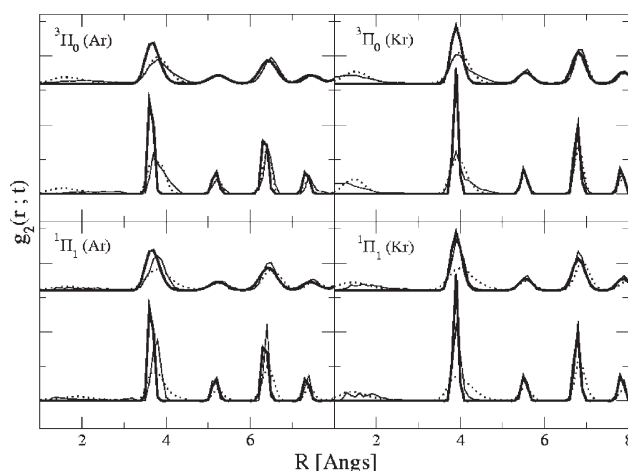


Fig. 13 The matrix atom radial distribution functions collected during the ground state evolution (thick line), and the pair correlation functions calculated from substitutional position during 0–500 fs ($^3\Pi_0$) or 0–100 fs ($^1\Pi_1$) after excitation (solid line) and the rest of excited state evaluation (dotted line). The bottom lines are the 5 K results and upper lines correspond to the scaled temperatures (46 K for Ar, 36 K for Kr).

partner behind the tetraatomic Ar window barely shows up because the other five second nearest neighbours remain unaffected. The closest coordination shell, instead, is clearly distorted upon excitation also in the well oriented Ar 5 K case. Apart from the different lattice size, the collisional changes in the two matrices are very similar. The detailed mechanisms are, however, quite the opposite, since the distortion of the closest shell increases with temperature in Ar, whereas in Kr more trajectories miss the direct collision as the initial angle distribution $\rho(\theta, \phi)$ spreads. The figure shows that the extent of atom dislocation broadens the nearest neighbour lines up to 0.5 Å, roughly. The Ar case shows also a peak shift of 0.1 Å between maxima of the static RDFs and the short-time pair-correlation functions, since more atoms are affected upon the window-oriented bond-stretch than in the direct collision. The traces of Cl and F atom movements in the 1–2 Å region are more visible in Kr due to faster recombination times after excitation.

Molecular dissociation remains a rare event in the calculated Kr case. For reference, we show the calculated ClF wavepacket construct $P(r, t)$ evolving after 387 nm and 308 nm excitations in Fig. 14. The Cl–F distance can grow large, though, in the second and later periods after excitation into the tetraatomic window at high temperatures. These represent close-to delayed dissociation, but no stable trapping sites can be found *via* this route. The single permanent dissociation found in the trajectories (graph (b) right panel) corresponds to excitation with $\theta, \phi = 25^\circ, 76^\circ$, three angle-scattering oscillations, and

subsequent cage exit at 1.3 ps through the triatomic window into the tetrahedral site. The computation method can not account for the probable formation of charge-transfer complexes between the halogens and Kr atoms, which may affect the dynamics to a large extent.

D. Alignment and pump excitation

We explore the fragment atom motions towards the triatomic window, absent in the free dynamics above, by applying the CW field described in Section III B. This window proves to be the main route for dissociation, and we present the results as energy-distance plots in Fig. 15. In Ar matrix we find direct dissociation at 308 nm excitation 46 times out of 50, visible by trapping of r_{ClF} between 3.5 and 5 Å. Delayed dissociations are not found but delayed recombinations do take place twice. The 387 nm excitation leads to coherent wave-packet motion where the first recombination from the window barrier results in opening of the cage and a lengthened second outward trajectory, followed by a shorter third oscillation. Seven delayed dissociations are observed in the fourth period, accompanied by suitable COM motion kicking fluorine over the window barrier. This is qualitatively close to motions in the tetraatomic window. The three first inner turning points are located approximately at 220, 510, and 700 fs showing a comparable time structure to the field-free case. It is noted that the breathing window acts as a geometrical lens, focusing the trajectories

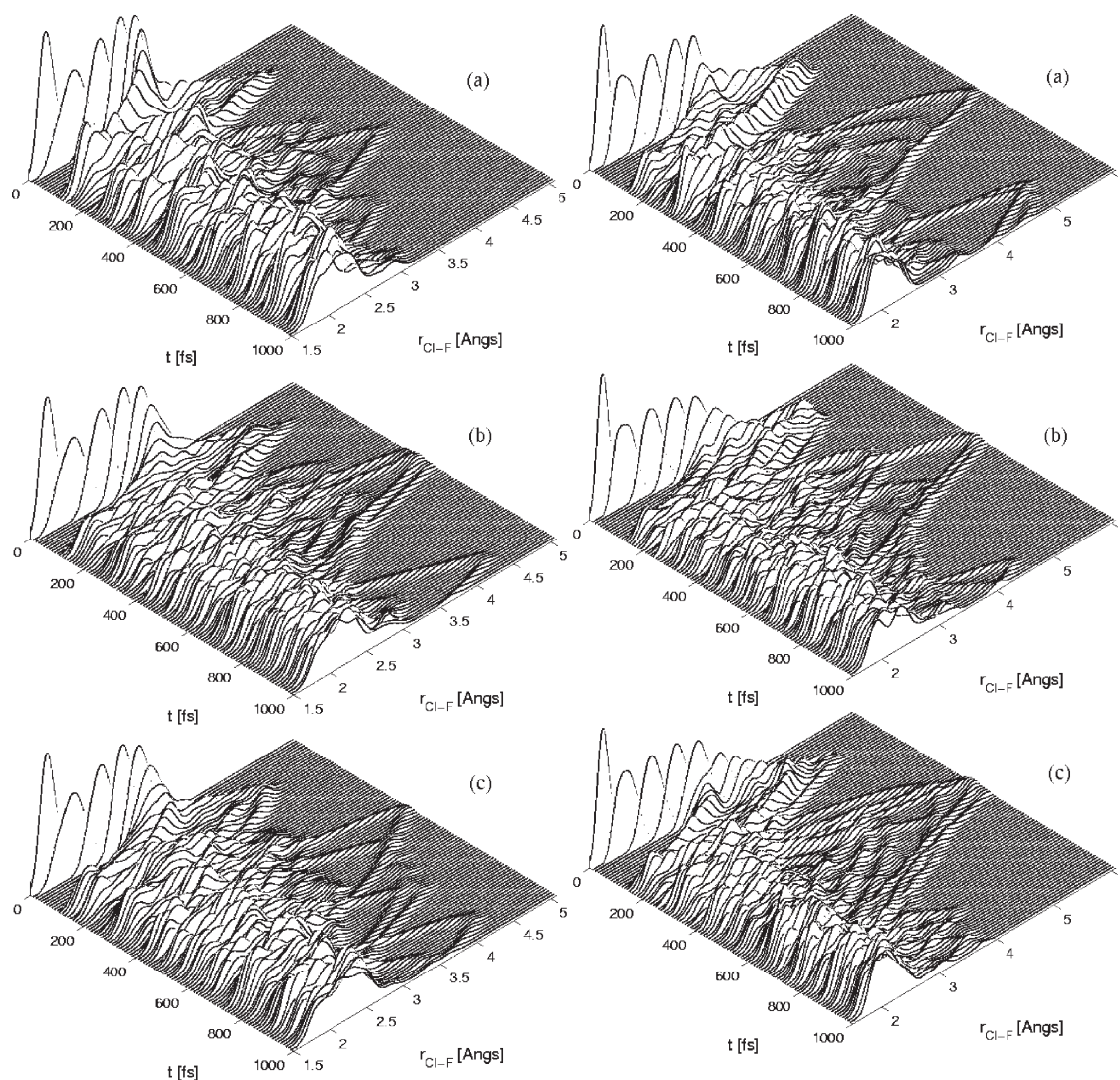


Fig. 14 Left: $P(r, t)$ of ClF in Kr for 387 nm excitation to the B state. Right: $P(r, t)$ of ClF in Kr for 308 nm excitation to the $^1\Pi_1$ state. Temperature: (a) 5 K; (b) 19 K; (c) 36 K.

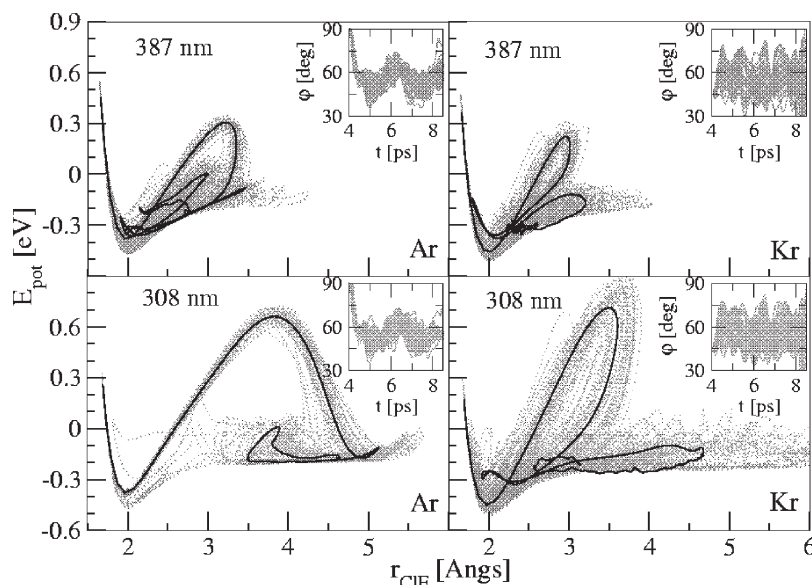


Fig. 15 Potential energy experienced by the molecule during 1 ps after excitation into the triatomic window plotted against the internuclear separation as in Fig. 11. The insets show the angle between the molecular axis and the laboratory x -coordinate during the ground state evolution with an external static field.

to the centre of the window and no notable bond rotation occurs during the first ps.

The lower excitation energy does not lead to dissociation events in Kr. What was discussed for Ar with 387 nm excitation applies also here for the first three oscillations, but instead of a delayed dissociation only bond rotation takes place. With the higher excitation energy the second stretch finally exits the cage which leads to permanent dissociation of the molecule with 50% probability. The insets in Fig. 15 show the degree of orientation attained by the intense field by presenting the Euler angle $\varphi = \cos^{-1}(\sin\theta\cos\phi)$ aimed at the desired 54.7 degrees. With the same external conditions the angular spread is $\delta\varphi \approx 30^\circ$ in both matrices. As the field was abruptly switched on at 4 ps, quick reorientation then follows and overshoots the target, leading to oscillations with *ca.* 2.5 ps period. This happens quite similarly for the members of the ensemble, and rather tight angular distribution, $\delta\varphi \approx 15^\circ$, is found in Ar at the moment of pump excitation after 8 ps. In Kr, the thermal orientation is already closer to the desired one and the $\sin\theta$ -dependent force term is smaller, leading to a smaller overshoot in the beginning.

IV. Summary

We inspected the ground state properties and photodynamics of the rare-gas embedded CIF molecule in this study. Several characteristic features were revealed, and we list them as follows.

(i) The preferred molecular orientation is towards a tetra-atomic cage window in Ar and towards a nearest neighbour atom, cage wall, in Kr. The triatomic window gives only a local rotational potential energy minimum (Ar) or maximum (Kr) in static lattices but this orientation is strictly avoided in the dynamical case in both solids. The reorientational dynamics observed at elevated temperatures is reduced to small librations at 5 K.

(ii) The low temperature leads to well-resolved wave-packet motion for 1 ps after photo-excitation to the $B^3\Pi_0$ or $^1\Pi_1$ states. Shortening of the round-trip times from the initial 330–410 fs to 160 fs periods is observed as the molecular oscillations change from out-cage to in-cage recombinative motion. Most of the excess energy is lost during the first bond stretch, and the collisions cause the matrix cage to expand and “breathe” with *ca.* 800 fs period. The relation of these time

scales to the experimental pump–probe spectra are given in the accompanying article.²⁶

(iii) Upon F fragment exiting the cage through the window, no stable trapping site is found between the first and second coordination shell atoms for permanent dissociation. At elevated temperatures, the orientation samples the cage volume to a larger extent; however, dissociation remains absent unless the higher pump pulse energy is used to excite the $^1\Pi_1$ state. A triatomic window is found for the dissociative route yielding a separated F atom in the nearest interstitial site of octahedral symmetry.

(iv) According to the present classical evaluations we find the rotational barriers too high to be overcome by an experimentally manageable ultrashort alignment field. We note, however, that the quantum barriers will be lowered by the zero-point librational energies in these wells. It is estimated²⁶ that this reduction can bring the barrier heights to the same order of magnitude that can be overcome by realistic field intensities, thus making the strong-field alignment scheme feasible. The present purpose is to study short pulses with respect to the rotational time-scale (32 ps for CIF), which has an advantage over the adiabatic regime *via* the possibility of field-free (post-pulse) alignment. Longer pulses in the adiabatic limit can however be used to make the alignment more effective.

Studies to unravel the nature of librational states and alignment in the solid state by time-dependent Schrödinger equation are in progress as a co-operation with Dr. B. Schmidt (Dept. of Mathematics, FU-Berlin). Furthermore, the analysis of stationary librational states is carried out in the forthcoming article along with a comparison to infrared spectroscopic data.²⁶ Enhancement of alignment in ultrashort regime may be attained using pulse trains, as discussed by Leibscher *et al.*,⁴⁵ where the sequential kicks dramatically narrow the rotor angular distribution in optimal case. Experiments are planned in our group to carry out the alignment-pump–probe scheme in a solid hydrogen matrix, which is expected to provide a softer and less hindering environment for the rotation of the impurity molecule.

Acknowledgements

Dr Burkhard Schmidt is gratefully acknowledged for insightful suggestions on the manuscript. T.K. has been supported by a

Marie Curie Fellowship of the European Community programme “Improving the Human Research Potential and the Socio-Economic Knowledge Base” under contract number HPMF-CT-2002-01854. This research is supported by the project “Analysis and control of ultrafast photoinduced reactions” (SFB 450) of the Deutsche Forschungsgemeinschaft (DFG).

References

- 1 J. Manz and L. Wöste, *Femtosecond Chemistry*, VCH Verlagsgesellschaft, Weinheim, 1995, vols. 1 and 2.
- 2 S. A. Rice and M. Zhao, *Optical Control of Molecular Dynamics*, John Wiley & Sons Inc., New York, 2000.
- 3 P. W. Brumer and M. Shapiro, *Principles of the Quantum Control of Molecular Processes*, Wiley-VCH, Weinheim, 2003.
- 4 D. J. Tannor, R. Kosloff and S. A. Rice, *J. Chem. Phys.*, 1986, **85**, 5805.
- 5 D. J. Tannor and S. Rice, *J. Chem. Phys.*, 1985, **83**, 5013.
- 6 P. Brumer and M. Shapiro, *Annu. Rev. Phys. Chem.*, 1992, **43**, 257.
- 7 P. Gross, D. Neuhauser and H. Rabitz, *J. Chem. Phys.*, 1993, **98**, 4557.
- 8 T. Brixner, N. H. Damrauer, P. Niklaus and G. Gerber, *Nature*, 2001, **414**, 57.
- 9 I. Sh. Averbukh, M. J. J. Vrakking, D. M. Villeneuve and A. Stolow, *Phys. Rev. Lett.*, 1996, **77**, 3518.
- 10 A. H. Zewail, *J. Phys. Chem. A*, 2000, **104**, 5660.
- 11 M. Bargheer, P. Dietrich and N. Schwentner, *J. Chem. Phys.*, 2001, **115**, 149.
- 12 M. Bargheer, M. Gühr and N. Schwentner, *J. Chem. Phys.*, 2002, **117**, 5.
- 13 R. B. Gerber, *Annu. Rev. Phys. Chem.*, 2004, 10.1146/annurev.physchem.55.091602.094420.
- 14 H. Stapelfeld and T. Seideman, *Rev. Mod. Phys.*, 2003, **75**, 543.
- 15 V. S. Batista and D. F. Coker, *J. Chem. Phys.*, 1996, **105**, 4033.
- 16 J. C. Tully, *J. Chem. Phys.*, 1990, **93**, 1061.
- 17 V. S. Batista and D. F. Coker, *J. Chem. Phys.*, 1997, **106**, 6923.
- 18 I. H. Gersonde and H. Gabriel, *J. Chem. Phys.*, 1993, **98**, 2094.
- 19 M. Y. Niv, M. Bargheer and R. B. Gerber, *J. Chem. Phys.*, 2000, **113**, 6660.
- 20 M. Bargheer, R. B. Gerber, M. V. Korolkov, O. Kühn, J. Manz, M. Schröder and N. Schwentner, *Phys. Chem. Chem. Phys.*, 2002, **4**, 5554.
- 21 M. V. Korolkov and J. Manz, *Z. Phys. Chem.*, 2003, **217**, 115.
- 22 G. Chaban, R. B. Gerber, M. V. Korolkov, J. Manz, M. Y. Niv and B. Schmidt, *J. Phys. Chem. A*, 2001, **105**, 2770.
- 23 R. B. Gerber, M. V. Korolkov, J. Manz, M. Y. Niv and B. Schmidt, *Chem. Phys. Lett.*, 2000, **327**, 76.
- 24 S. Fernandez Alberti, J. Echave, V. Engel, N. Halberstadt and J. A. Beswick, *J. Chem. Phys.*, 2000, **113**, 1027.
- 25 S. Fernandez Alberti, N. Halberstadt, J. A. Beswick, A. Bastida, J. Zúñiga and A. Requena, *J. Chem. Phys.*, 1999, **111**, 239.
- 26 T. Kiljunen, M. Bargheer, M. Gühr, N. Schwentner and B. Schmidt, *Phys. Chem. Chem. Phys.*, 2004, **6**, 10.1039/b401437e.
- 27 R. A. Aziz and M. J. Slaman, *Mol. Phys.*, 1986, **58**, 679.
- 28 A. B. Alekseyev, H.-P. Liebermann, R. J. Buenker and D. B. Kokh, *J. Chem. Phys.*, 2000, **112**, 2274.
- 29 V. Aquilanti, E. Luzzatti, F. Pirani and G. G. Volpi, *J. Chem. Phys.*, 1988, **89**, 6165.
- 30 V. Aquilanti, D. Cappelletti, V. Lorent, E. Luzzatti and F. Pirani, *J. Phys. Chem.*, 1993, **97**, 2063.
- 31 M. P. Allen and D. J. Tildesley, *Computer Simulation of liquids*, Clarendon Press, Oxford, 1987.
- 32 E. Hairer, C. Lubich and G. Wanner, *Geometric Numerical Integration. Structure-Preserving Algorithms for Ordinary Differential Equations*, Springer, Berlin, 2002.
- 33 J. P. Bergsma, P. H. Berens, K. R. Wilson, D. R. Fredkin and E. J. Heller, *J. Phys. Chem.*, 1984, **88**, 612.
- 34 C. Kittel, *Introduction to Solid State Physics*, Wiley, New York, 7th edn., 1996.
- 35 H. J. C. Berendsen, J. P. M. Postma, W. F. van Gunsteren, A. DiNola and J. R. Haak, *J. Chem. Phys.*, 1984, **81**, 3684.
- 36 B. Friedrich and D. Herschbach, *Phys. Rev. Lett.*, 1995, **74**, 4623.
- 37 B. Fabricant and J. S. Muentner, *J. Chem. Phys.*, 1977, **66**, 5274.
- 38 J. Ortigoso, M. Rodríguez, M. Gupta and B. Friedrich, *J. Chem. Phys.*, 1999, **110**, 3870.
- 39 A. Cenian and H. Gabriel, *J. Phys.: Condens. Matter*, 2001, **13**, 4323.
- 40 M. Bargheer, M. Y. Niv, R. B. Gerber and N. Schwentner, *Phys. Rev. Lett.*, 2002, **89**, 108 301.
- 41 M. L. Klein and J. A. Venables, *Rare Gas Solids*, Academic Press, New York, 1977, vol. II.
- 42 K. S. Kizer and V. A. Apkarian, *J. Chem. Phys.*, 1995, **103**, 4945.
- 43 R. Kometer, PhD Thesis, FU-Berlin, 1995.
- 44 J. G. McCaffrey, H. Kunz and N. Schwentner, *J. Chem. Phys.*, 1992, **96**, 2825.
- 45 M. Leibscher, I. Sh. Averbukh and H. Rabitz, *Phys. Rev. Lett.*, 2003, **90**, 213001.